Received: 18 April 2023 | Revised: 3 July 2023 | Accepted: 15 August 2023

DOI: 10.4218/etrij.2023-0156

ORIGINAL ARTICLE

ETRI Journal WILEY

Performance analysis of atomic magnetometer and bandwidth-extended loop antenna in resonant phase-modulated magnetic field communication system

Hyun Joon Lee | **Jung Hoon Oh** | **Jang-Yeol Kim** | **In-Kui Cho**

Radio Research Division, Electronics and Telecommunications Research Institute, Daejeon, Republic of Korea

Correspondence
In-Kui Cho, Radio Research Division, Electronics and Telecommunications Research Institute, Daejeon, Republic of Korea.
Email: cho303@etri.re.kr

Funding information
Institute of Information & Communications Technology Planning & Evaluation (IITP), Korea Government (MSIT), Grant/Award Number: 2019-0-00007

Abstract

Telecommunications through an electrically conductive medium require the use of carrier bands with very-low and ultralow frequencies to establish radio-frequency links in harsh environments. Recent advances in atomic magnetometers operating at very-low frequencies have facilitated the reception of digitally modulated signals. We demonstrate the transmission and reception of quadrature phase-shift keying (QPSK) signals using a multi-resonant loop antenna and atomic magnetometer, respectively. We report the measured error vector magnitude according to the symbol rate for QPSK modulation and analyze the bandwidth of a receiver based on the atomic magnetometer. The multi-resonant loop antenna noticeably enhances the bandwidth by over 70% compared with a single-loop antenna. QPSK modulation for a carrier frequency of 20 kHz and symbol rate of 150 symbols per second verifies the feasibility of demodulation, and the measured error vector magnitude and signal-to-noise ratio are 7.29% and 30.9 dB, respectively.

KEYWORDS
antenna optimization, atomic magnetometer, communication, magnetic field, multi-resonant loop antenna

1 | INTRODUCTION

Magnetic fields are fundamental and observable physical quantities that provide valuable insights into diverse electromagnetic phenomena. Research on ultrasensitive magnetometers has been actively conducted for diverse applications, including the investigation of fundamental physical symmetries [1, 2], geophysical studies [3, 4], and low-field nuclear magnetic resonance as well as magnetic resonance imaging [5–9]. In recent years, communication technologies that employ magnetic fields in the radio-frequency (RF) band have emerged to extend the communication space. These technologies have been applied to different areas, such as underwater, underground, and short-range Internet of Things, with fundamental principles and technical overviews including channel models and protocol designs being developed [10–12]. In sensor-based technology, conventional antenna-based receivers are being gradually replaced by magnetometers, such as induction coils with ferrite cores [13], giant magnetoimpedance-based sensors [14], and atomic magnetometers [15–18]. Such magnetometers exhibit compactness, cost effectiveness, and high magnetic sensitivity. In particular, atomic magnetometers can

extend the signal range by implementing balanced detection that allows measuring circularly polarized RF signals while reducing linearly polarized noise [17]. Furthermore, atomic magnetometers allow to modulate or demodulate the polarization helicity of a magnetic field, enabling a new communication approach [18].

Communications generally rely on the generation, transmission, and reception of electromagnetic waves. When generating electromagnetic waves, an adequate signal frequency is essential for efficient interconnection between channels. This is because the electromagnetic wave propagation can be disrupted or completely obstructed in specific environments. For example, time-varying magnetic fields are susceptible to exponential attenuation when propagating through highly conductive media, such as seawater [19]. This attenuation depends on the skin depth of the modulated magnetic field, which is in turn determined by the conductivity, object permeability, and applied frequency. Therefore, the use of low-frequency electromagnetic signals is imperative for achieving robustness to signal attenuation. Recent studies have demonstrated the feasibility of radio communication for carrier frequencies in the very low frequency band (<40 kHz), which reduces attenuation [13, 14].

For transmission, bidirectional communication requires a compact antenna design regardless of the operation wavelength. This is typically achieved using narrowband resonant structures to improve the power efficiency [20]. A resonant loop antenna generates a magnetic field at a specific frequency determined by its matching capacitance and not by its diameter [11]. Hence, loop antennas are compact and enable mobile magnetic induction links [2, 14]. For reception of electromagnetic waves, receiver characteristics such as the signal-to-noise ratio (SNR) should be determined. Atomic magnetometers operating in self-oscillating mode have been used to detect and receive communication signals that suffer from strong attenuation [15]. An increased range has been achieved by exploiting a low noise level (below 1 $pT/Hz^{1/2}$) of the magnetometer when employing binary phase-shift keying (BPSK) signals. However, a self-oscillating magnetometer has inherent operating bandwidth limitations, restricting the communication channel capacity. Among available atomic magnetometers, the RF atomic magnetometer (RFAM) is the most versatile for communication and applications [21–25]. It exhibits exceptional sensitivity in unshielded measurements, and its operating frequency can be conveniently tuned by regulating the bias field around atoms. Additionally, it can resonantly detect oscillating fields within a narrow bandwidth while excluding broadband environmental noise [22, 24].

Most existing studies have been limited to amplitude and frequency modulation schemes [15, 16]. A widely used modulation scheme for data transmission is the phase modulation of carrier waves. Most digital modulation schemes, such as BPSK, quadrature phase-shift keying (QPSK), and quadrature amplitude modulation, detect and receive carrier-phase-modulated signals, for which the phase of the carrier RF signal must be detected. Before evaluating RFAM receivers and comparing them with conventional systems for receiving phase-modulated signals, their ability to detect and receive data using such modulation schemes should be demonstrated.

In this study, we investigated the use of RFAMs in communication for phase-modulated signal reception. We used RFAMs in the detection of a phase-modulated RF carrier as well as the detection and reception of QPSK signals. We used an RFAM based on ^{85}Rb vapor, which is sensitive to the phase and amplitude of a resonant RF magnetic field, and evaluated an RF communication link using QPSK modulation. The RFAM had a noise floor of 300 $fT/Hz^{1/2}$ and a bandwidth of 300 Hz. Furthermore, a transmitter (T_x) comprising a multi-resonant loop antenna with several narrowband resonant-loop antennas was developed. The proposed T_x expanded the bandwidth by more than 70% compared with a single-loop antenna for a bandwidth of approximately 1 kHz.

2 | SYSTEM CONFIGURATION

A schematic of the experimental setup for the magnetic-field-based communication system implemented in this study is shown in Figure 1. The corresponding system includes three major components: (1) RFAM, which serves as the magnetic sensor for phase-modulated signal reception; (2) multi-resonant loop antenna that generates RF signals; and (3) digital data encoding/decoding system.

2.1 | RFAM

We used an atomic magnetometer as the receiver that operates according to the RF resonance of the Zeeman transition in the ground state. A cubic cell (15 mm × 15 mm × 15 mm) containing ^{85}Rb vapor and 20 Torr of N_2 buffer gas was placed in a rectangular oven composed of boron nitride, a high-temperature ceramic. The oven heated the cell up to 70°C through a resistive heater constituted by an anti-inductive printed electrode supplied with an AC current of 1.0 MHz, which was far from the resonance range of the magnetometer. At 70 ± 0.5°C, the atomic density of Rb was

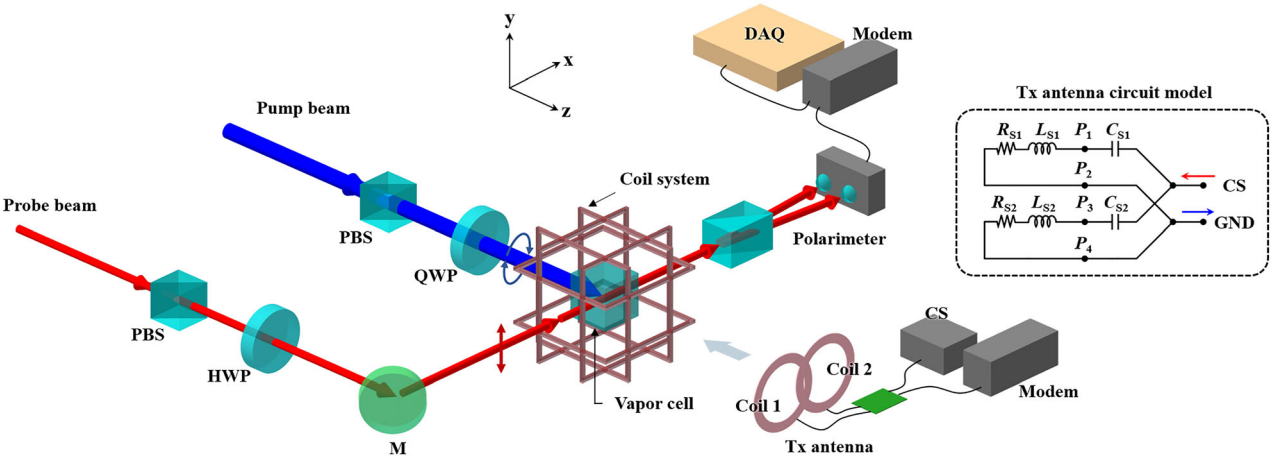

FIGURE 1 Schematic of T_x antenna, atomic-magnetometer-based sensor, and modems for magnetic field communication. A pump beam (blue) is delivered by an ^{85}Rb D_1 line laser (795 nm), and a probe beam (red) is delivered by a D_2 line laser (780 nm). The T_x antenna consists of resonant loop coils arranged in a single-layered flat spiral configuration with connection to the output of a current source. The modems encode digital signals transmitted by the T_x antenna and decode the signals received by the atomic-based sensor. The dashed box shows the equivalent circuit model of the T_x antenna. CS, current source; DAQ, data acquisition system; GND, ground; HWP, half-wave plate; PBS, polarizing beam splitter; QWP, quarter-wave plate.

computed to be approximately 7×10^{11} cm^{-3}. The precision magnetic-field coil system comprised three axial Helmholtz and anti-Helmholtz coils. The Larmor frequency (ω_L) was established by a bias DC magnetic field (B_{DC}) aligned along the z axis according to $\omega_L = \gamma B_{DC}$, where γ is the gyromagnetic ratio of the Rb atom. The homogeneity of field B_{DC} was enhanced by suppressing the magnetic field gradient using a first-order gradient coil. The magnetometer was calibrated by subjecting it to a well-defined test field along the y axis to handle the spin coherence between ground states. The cell and coil systems were placed inside a four-layer set of cylindrical mu-metal chambers operated with the end caps removed. The measured ambient magnetic field in an open laboratory environment containing the RFAM was 38.87 μT, as measured by a triaxial fluxgate magnetometer (Bartington Mag-03, Oxford, United Kingdom). This field was compensated for using Helmholtz coils driven by three independent current sources with a noise of 3 nA/Hz$^{1/2}$.

The optical configuration was applied to a 794.97 nm pump laser ($F = 2 \rightarrow F' = 3$ transition of ^{85}Rb D_1 line) and 780.22 nm probe laser (blue-detuned away from ^{85}Rb D_2 line). Diode lasers with external cavities (Toptica DL Pro; Bayern Gräfelfing, Bayern, Germany) were used, and the diode currents and temperatures were controlled using digital controllers (Toptica DLC; Bayern Gräfelfing). Atomic spin polarization was achieved by using a circularly polarized pump laser propagating along the z axis. The beam was extended to a diameter of 3 mm by passing it through two lenses to provide an adequately large sensing volume. A linearly polarized probe beam propagating along the x axis was blue-detuned from the ^{85}Rb D_2 line by 5 GHz to minimize the atomic spin disturbance caused by probe beam absorption.

The transverse spin polarization created by a resonant RF magnetic field (B_{rf}) generated by a test coil (y-axis coil in the Helmholtz coil) was obtained via the Faraday rotation of the linearly polarized probe beam. After passing through a polarizing beam splitter, half-wave plate, and Rb vapor cell, the probe beam entered a balanced polarimeter with an analyzer and photodiodes. The laser beam was divided into two paths with orthogonal polarizations, and the difference between the signals on the photodiodes was measured. The rotational signal (V_{out}) was examined using a data acquisition system consisting of an SR860 lock-in amplifier (SRS, San Francisco, CA, United States) and an FSV spectrum analyzer (Rohde & Schwarz, Munich, Germany). The lock-in amplifier extracted the signal components in a rectangular form, both out (dispersive) and in phase (absorptive), enabling phase-sensitive detection with a reference from the source of B_{rf}. The spectrum analyzer measured the spectral power of the known and unknown signals by scaling the magnitude of the input signal according to frequency.

2.2 | Multi-resonant loop antenna

The T_x antenna was composed of two loop coils (Coils 1 and 2, as shown in Figure 1) with slightly different resonant frequencies. Each coil was formed as a

single-layered flat spiral with an inner diameter of 0.16 m and 20 turns. The winding consisted of 700 strands of 40 AWG Litz wires with a diameter of 3 mm.

Because the operating frequency of the loop coil was substantially lower than its self-resonant frequency, we modeled it as a series-connected circuit comprising an inductor and resistor. As shown in the box of Figure 1, the T_x antenna model comprised inductors (L_{s1} and L_{s2}) and wire resistors (R_{s1} and R_{s2}). Because the self-resonant frequencies of the loop coils were 3.4 MHz and 3.7 MHz, applying matching capacitors (C_{s1} and C_{s2}) to the simplified model allowed to manipulate the resonant frequency according to $f_{c1,2} = 1/\sqrt{L_{s1,2}\, C_{s1,2}}$.

The frequency responses of $L_{s1,2}$ and $C_{s1,2}$, which ranged from 19 kHz to 21 kHz, are shown in Figure 2. At 19.7 kHz and 20.0 kHz for the loop coils, the corresponding values of L_{s1} and L_{s2} were 117 μH and 119 μH, respectively, while those of C_{s1} and C_{s2} were 542 pF and 549 pF, respectively. After addition of C_{s1} and C_{s2}, f_{c1} and f_{c2} were evaluated by measuring their quality factors (Q). At resonance, the circuit impedance approaching zero resulted in Q close to zero at frequency f_c, and f_{c1} and f_{c2} were 19.93 kHz and 19.74 kHz, respectively. The bandwidths of Coils 1 and 2 were 0.45 kHz and 0.49 kHz, respectively, at the 3 dB level. The geometric and electrical parameters of the loop coils are listed in Table 1.

Using this configuration, we aimed to extend the bandwidth and improve the power efficiency using multi-resonant loop coils. The mutual inductance (M) between the coils was thoroughly examined. To determine M, the following sequence of measurements was performed. The inductance (L_x) between Ports 1 (P_1) and 4 (P_4) was measured by binding Port 2 (P_2) to port 3 (P_3). Next, the inductance (L_y) between Ports P_1 and P_3 was measured by connecting Ports P_2 to P_4. Finally, M was computed as $(L_x - L_y)/4$.

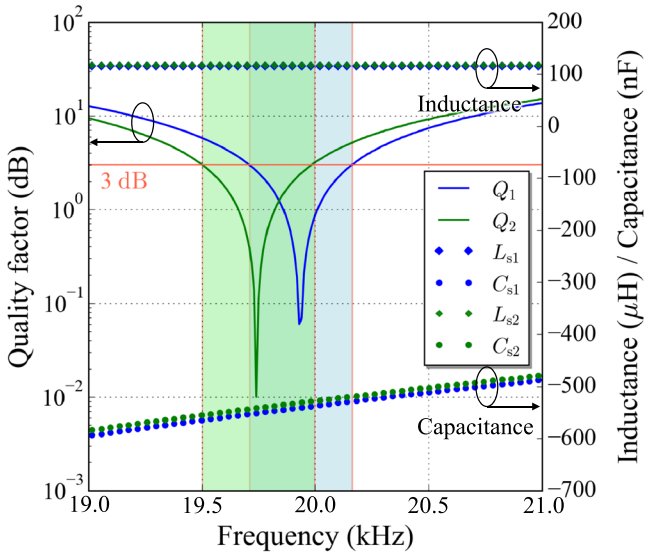

FIGURE 2 Measured inductance, capacitance, and quality factor of Coils 1 and 2 according to frequency. The resonant frequencies of Coils 1 and 2 are 19.93 kHz (blue solid line) and 19.74 kHz (green solid line), respectively, and their bandwidths are 0.45 kHz (blue shading) and 0.49 kHz (green shading), respectively.

TABLE 1 Geometric and electrical parameters of loop coils.

Structure	Coil 1 Single-layered flat spiral	Coil 2 Single-layered flat spiral
Inner/outer diameter (m)	0.16/0.28	0.16/0.28
No. of turns	20	20
Self-resonant frequency (MHz)	3.4	3.7
Matching capacitance (pF)	542	549
Resonance frequency (kHz)	19.93	19.74
3 dB bandwidth (kHz)	0.45	0.49

2.3 | Digital data encoding and decoding

The modem shown in Figure 1 encoded and decoded keyed data. The system used a direct digital synthesizer (PXIe-5442; NI, Austin, TX, United States) to generate modulated digital signals and a digital oscilloscope (PXIe-5122; NI) to digitize the analog-modulated RF signals. The data bits were encoded at f_c near the RFAM Larmor frequency using QPSK modulation, with symbols represented by carrier phase shifts of $\pm\pi/4$ rad. Frequency f_c was set to 20 kHz, that is, the resonant frequency of the multi-resonant antenna (T_x antenna in Figure 1). The symbol rate was adjusted from 50 Hz to 400 Hz. Furthermore, the system was equipped with a software test platform implemented in the LabVIEW software (NI), which efficiently corrected any decoding errors, thus facilitating the recovery of the original digital data.

3 | RESULTS AND DISCUSSION

3.1 | Atomic magnetometer response

Figure 3A shows the measured in-phase and quadrature components of rotation signal V_{out} in response to B_{rf} in frequencies close to ω_L, and Figure 3B shows the oscillations obtained from the balanced polarimeter at the resonant frequency. The on-resonant frequency was close to

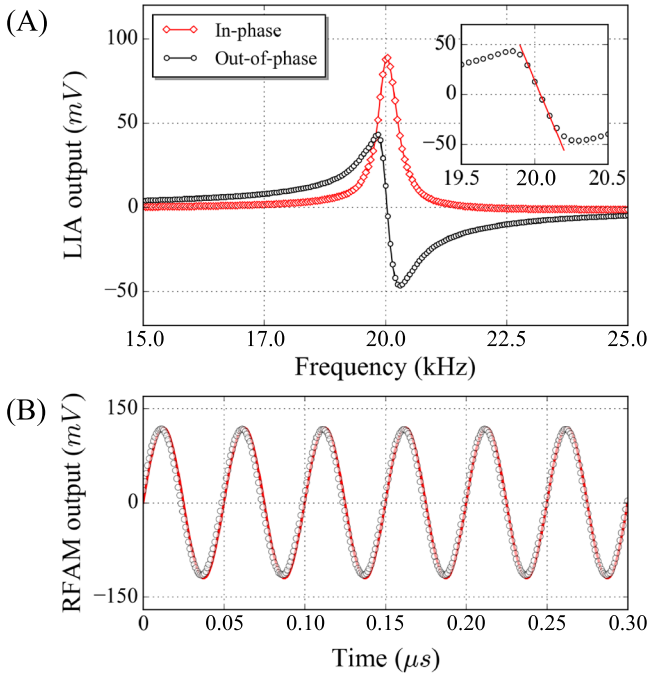

FIGURE 3 Resonance response of magnetometer under optimal conditions. (A) Typical out-of-phase (black circles) and in-phase (red diamonds) responses of magnetometer near 20 kHz ($B_{DC} = 4.29$ μT, $\gamma = 4.69$ kHz/μT for ^{85}Rb). The inset shows the optical rotation in a near-resonance linear fit. LIA, lock-in amplifier. (B) Output of polarimeter (black circles) at resonant frequency and fitted with a sine wave of 20.0 kHz (red solid line). Near-optimal conditions: pump intensity, 50 mW/cm^2; probe intensity, 9.5 mW/cm^2; vapor cell temperature, 70°C.

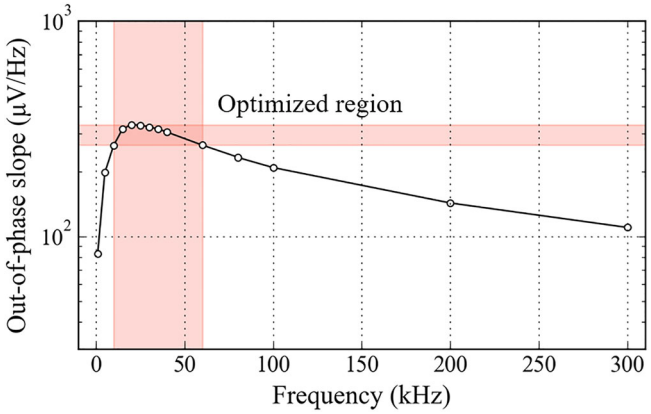

FIGURE 4 Magnetometer in-phase slopes according to applied B_{rf} frequency. From 10 kHz to 60 kHz, the slope varies from 265 μV/Hz to 330 μV/Hz (shaded region), with the maximum observed at 20 kHz.

20 kHz, corresponding to $B_{DC} = 4.29$ μT ($\gamma = 4.69$ kHz/μT for ^{85}Rb). The sensitivity of an atomic magnetometer is proportional to the slope of the quadrature signal near resonance. To retain the highest sensitivity, the peak-to-peak amplitude and spectral width of the lock-in amplifier output were experimentally observed by adjusting the tunable parameters to maximize the dispersion curve slope. Under the experimental conditions, the laser intensities of the pump and probe beams were estimated as 50 mW/cm2 and 9.5 mW/cm^2, respectively.

Figure 4 illustrates the tunability of the operating frequency achieved under the optimal conditions of 20 kHz for practical applications. The results were obtained for frequencies of 1 kHz–300 kHz, corresponding to a B_{DC} spread of 0.21 μT–63.97 μT. The maximum sensitivity was achieved from 10 to 60 kHz. The decrease in the slope for frequencies higher than 200 kHz was due to the broadening of the atomic response caused by the second-order Zeeman effect. Notably, the RFAM exhibited consistent sensitivity from 10 kHz to 40 kHz, and the increase in technical noise was confined to frequencies below 10 kHz. Furthermore, the developed RFAM demonstrated linear response characteristics in very-low frequencies, which were thus suitable for measuring signals.

The phase difference (θ) between V_{out} and B_{rf} was evaluated under on- and off-resonance conditions at frequencies tuned by field B_{DC}. As the operating bandwidth of RFAM was optimized from 15 kHz to 25 kHz, B_{DC} was set to the corresponding range from 3.21 μT to 5.36 μT (x axis in Figure 5). The lock-in responses of the RFAM to a reference synchronized to B_{rf} showed that its output was proportional to $V_{out}\cos(\theta)$, where θ is indicated as the blue curve in Figure 5. At resonance with $B_{DC} = 4.29$ μT, V_{out} achieved its maximum amplitude of 96 mV$_{rms}$, and θ approached zero, exactly matching both the precession frequency of the atoms and input RF frequency. When B_{DC} was detuned far from resonance, V_{out} and θ exhibited nonlinear convergence toward zero and ±90°, respectively. When B_{DC} ranged from 4.15 μT to 4.43 μT, the slope of the signal was approximately 180°/μT, corresponding to 38.3°/kHz. Therefore, an accurate B_{DC} setting was essential for improving the accuracy of phase measurement.

Figure 6 shows the frequency spectrum measured at approximately 20 kHz. To assess the noise level of the RFAM, we used the calibration peaks of a small oscillating field of 4.5 nT using a test coil. The observed resonant noise floor was approximately 300 fT/Hz$^{1/2}$, which was dominated by environmental magnetic and white noise components (e.g., photon-shot and atomic spin-projection noise components). Under a constant probe intensity, the photon-shot noise became the major noise contributor owing to the sufficiently high probe beam power, resulting in nearly constant noise. Furthermore, although the total noise was comparable to the spin-projection noise, the photon-shot noise increased owing to the absorption of the probe beam. Consequently, under

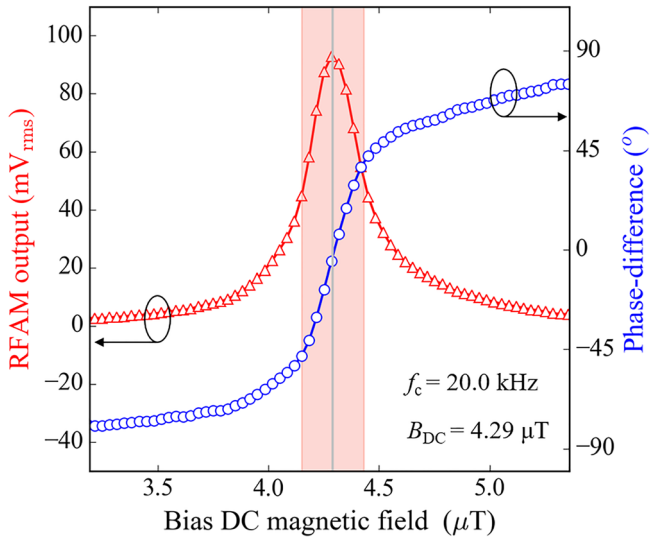

FIGURE 5 Phase-difference measurement according to B_{DC}. At $B_{DC} = 4.29$ μT, RFAM output V_{out} reaches its maximum, while θ approaches zero. The full width at half maximum of V_{out} is indicated by the shaded region, where θ undergoes a rapid linear transition.

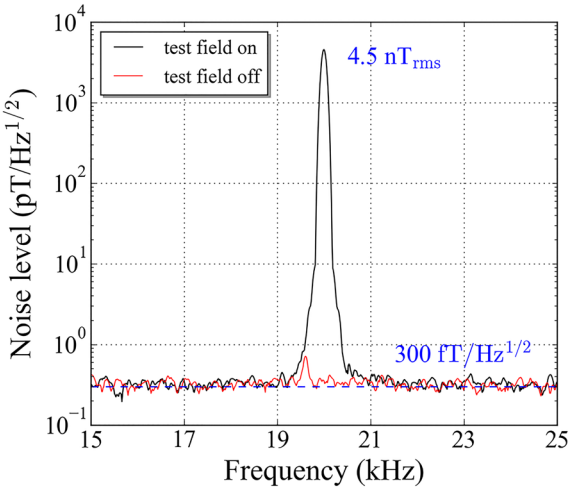

FIGURE 6 Magnetometer noise around 20 kHz measured by spectrum analyzer at 70°C with other parameters optimized. The noise was measured with (solid black line) and without (solid red line) a test field. The dashed blue line represents the total noise level of 300 fT/Hz$^{1/2}$.

our experimental conditions, the dominant noise component was the photon-shot noise. Signal enhancement can be achieved by adjusting the intensity of the probe beam and detuning it to mitigate depolarization. Nevertheless, because altering these parameters may affect the total noise, the tradeoff should be analyzed to achieve the optimal sensitivity.

3.2 | Optimization of T_x antenna

The mutual inductance (M) characterizes the relation between two magnetically coupled coils. It specifies the proportion of time-varying magnetic flux generated by a coil that induces a current in an adjacent coil. Thus, mutual inductance M between the two coils varies drastically depending on the coil positions.

Figure 7A shows the measurements of inductance M according to distance d between the centers of Loop Coils 1 and 2. We obtained 102 μH when the two coils overlapped perfectly (i.e., $d = 0$ cm). As d increased, M decreased sharply until it reached zero at $d = 16$ cm. For 16 cm–50 cm, M was negative, indicating that the current vectors of the two coils pointed in opposite directions. The position and orientation of the two coils influenced the current in Coil 1 and created a negative magnetic flux in Coil 2, whereas the mutual voltage in Coil 2 became negative. A negative M value did not necessarily indicate capacitance; however, for inductors like coils, it can be interpreted as capacitance when not operating in resonance. The minimum value was reached at $d = 20$ cm, after which M began to increase again and eventually converged to zero at $d = 50$ cm. Hence, we fixed the two loop coils constituting the T_x antenna at $d = 16$ cm to obtain $M = 0$ H. This allowed for a reduction in the surface area of the T_x antenna by approximately 80% compared with the case for $d \geq 50$ cm, which also provided $M = 0$ H.

To validate the coil design through M measurements, quality factor Q of the T_x antenna was obtained using an analogous method. Figure 7B shows the frequency characteristics obtained by measuring Q while varying d. When $M = 0$ H ($d = 16$ cm, as shown in Figure 7A), the resonant frequencies of Coils 1 and 2 were adjacent. As d increased ($M < 0$ H, i.e., under capacitance), the resonant peaks moved away from f_c and secondary peaks appeared. The maximum frequency separation between the peaks was observed at $d = 20$ cm. This was due to the presence of mutual inductance between the loops in addition to their own inductance. At $d = 16$ cm, inductive decoupling was achieved by overlapping two adjacent coils, whereas at $d = 20$ cm, the coils were capacitively coupled, leading to multiple fluctuations in the capacitance owing to negative M values and changing the resonant frequencies.

After optimizing the position of the two coils to $d = 16$ cm, we evaluated the T_x antenna bandwidth, which determined the channel capacity. Specifically, the current flow into the antenna was measured while applying an alternating current to the transmitting antenna at intervals of 0.1 kHz in 18 kHz–20 kHz. Normalization of the measured current yielded the results shown in

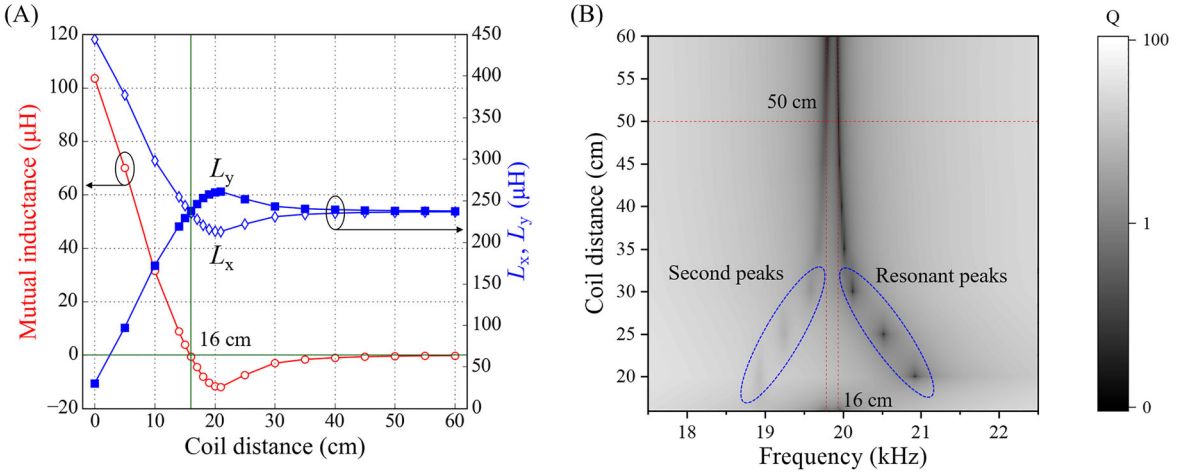

FIGURE 7 Measurements of (A) mutual inductance M and (B) quality factor Q according to coil distance d.

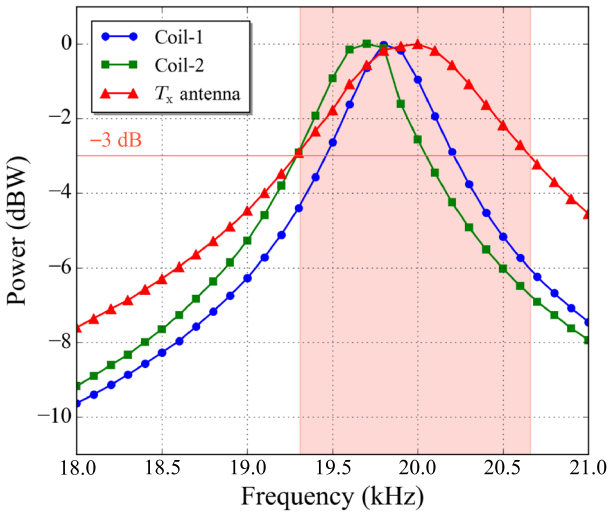

FIGURE 8 Power consumption according to input current frequency in Coils 1 and 2 as well as T_x antenna. The shading represents the T_x antenna bandwidth, indicating an extension of approximately 70% compared with the bandwidths of Coils 1 and 2.

Figure 8, with the maximum currents observed at 19.83 kHz, 19.69 kHz, and 20 kHz for Coils 1 and 2 and the T_x antenna, respectively. Defining the bandwidth as the point at which power was −3 dBW, Coils 1 and 2 and the T_x antenna exhibited bandwidths of 0.72, 0.71, and 1.35 kHz, respectively. The measured bandwidth suitably agreed with the results shown in Figure 7B but deviated from the predicted f_c value given the parasitic RLC components of the current measurement circuitry. Nonetheless, we verified that the multi-resonant loop antenna reached its maximum bandwidth when the mutual coupling between the two coils was zero, thereby extending the bandwidth by over 70% compared with a single-coil antenna.

3.3 | Communication performance

The error vector magnitude (EVM) is an important metric for evaluating the performance of digital communication systems because it directly influences the bit error rate and overall system performance. The EVM is commonly used along with other metrics, such as the SNR, to comprehensively evaluate digital communication systems. The PXIe-5122 device can generate an in-phase/quadrature diagram of the detected signal and calculate the EVM of the received bit stream.

Figure 9A shows the in-phase and quadrature diagrams for receiving data from the RFAM receiver under QPSK modulation at $f_c = 20$ kHz and a symbol rate of 150 symbols per second (sym/s). The measured SNR per bit and EVM were 30.6 dB and 7%, respectively. The T_x antenna was placed at 5 m from the RFAM in line of sight with its aperture along the z axis. The power consumption incurred during the transmission was estimated at 0.45 W, while the corresponding magnitude of the magnetic field measured beside the vapor cell was approximately 4 nT. Table 2 lists the receiver performances of the magnetic-field-based communication systems. The atomic-based receiver had a DC frequency band of 1 kHz [15]. This approach reduced the operating range in terms of the skin effect. Moreover, BPSK modulation mitigated the influence of environmental noise. However, this method was limited regarding the achievable data rate. A magnetic induction coil generally exhibits lower magnetic sensitivity than atom-based receivers [13], thereby imposing constraints on the

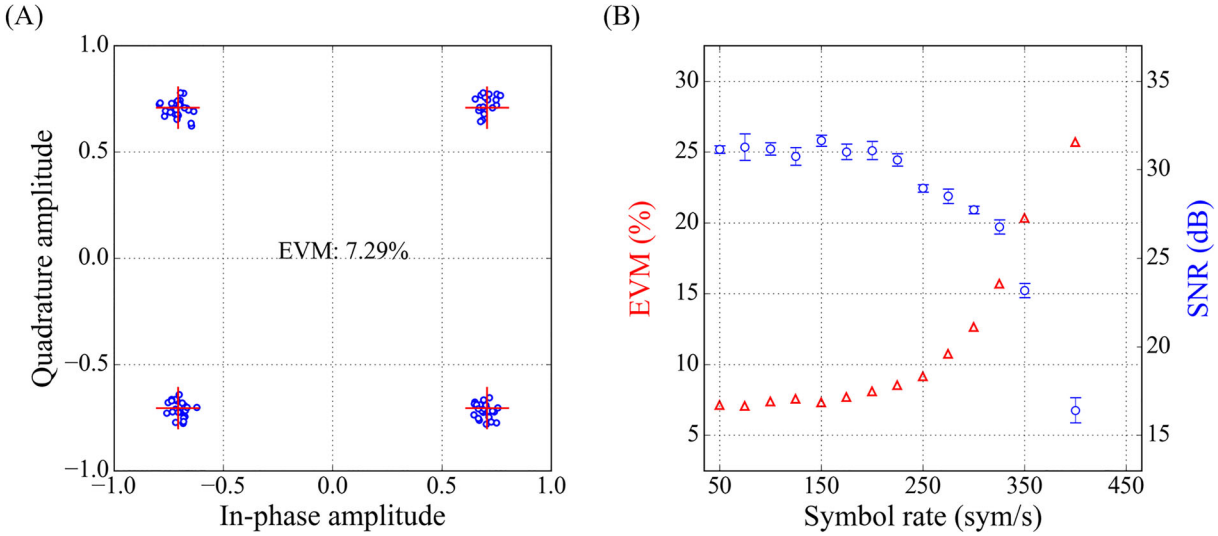

FIGURE 9 (A) Measured in-phase/quadrature diagram under QPSK modulation at $f_c = 20$ kHz with corresponding EVM. (B) Measured EVM and SNR according to symbol rate under QPSK modulation.

TABLE 2 Receiver performance in magnetic-field-based communications.

Receiver type	RFAM (this study)	DC mode atomic magnetometer [15]	Magnetic induction coil [13]
Frequency band (kHz)[a]	10–60	DC-1	5–35
Noise level (pT/Hz$^{1/2}$)	0.3	1.4	1.68
Modulation	QPSK	BPSK	QPSK
Carrier frequency (kHz)	20	0.210	20
Communication performance			
Data rate (bps)	300	30	2000
EVM (%)	7.6	–	5.6
SNR (dB)	30.6	26	30.6

[a]Range of radio frequencies used to receive signals under optimal conditions.

communication range. Hence, the frequency band and inherent noise characteristics of the employed RFAM offer advantages for communication range and data rate.

Figure 9B shows the EVM and SNR according to the symbol rate; they remained below 10% and above 25 dB, respectively, for symbol rates from 50 sym/s to 250 sym/s. However, for symbol rates greater than 250 sym/s, the EVM gradually increased and reached 27% at 400 sym/s. According to the EVM required for QPSK modulation [26], the maximum estimated symbol rate was approximately 350 sym/s. The bandwidth of the RFAM receiver was constrained by the coherence lifetime of the atomic spins, which determined the linewidth observed in spectroscopic measurements. The sensitivity of an RFAM is directly proportional to the slope of the dispersion curve. Its bandwidth depends on tunable parameters, such as the intensities of the pump and probe beams, and external factors, such as external magnetic fields, including those of the Earth. Optimizing the performance requires a careful balance between sensitivity and bandwidth, which must be determined empirically according to the communication environment.

Overall, our findings can be summarized as follows:

- We evaluated the properties of a multi-resonant loop antenna by measuring the mutual inductance and power consumption according to the positions of its two coils. The analysis resulted in the development of a compact low-power antenna operating in very-low frequencies and exhibiting an approximate increase of 70% in bandwidth compared with a single-loop antenna.
- The phase-modulated signal transmitted by the multi-resonant antenna was successfully received by the RFAM in a partially magnetically shielded environment. The sensitivity of the RFAM was optimized in

very-low frequencies by measuring optical rotation signals, achieving a noise floor of 300 fT/Hz$^{1/2}$.
- The measured EVM and SNR were 7% and 30.6 dB, respectively, at 150 sym/s.

4 | CONCLUSIONS

We investigated the transmission and reception of phase-modulated signals from magnetic fields using multi-resonant antennas and an RFAM. The properties of the multi-resonant antenna were evaluated by measuring the mutual inductance and power consumption for different coil positions. Hence, we developed a compact low-power antenna operating in very-low frequencies with an approximate increase of 70% in bandwidth compared with a single-loop antenna. The phase-modulated signal transmitted by the multi-resonant antenna was received by the RFAM in a partially magnetically shielded environment. The sensitivity of the RFAM was optimized for a very-low-frequency band by measuring optical rotation signals with a noise floor of 300 fT/Hz$^{1/2}$. Optimization revealed that the photon-shot noise was the main contributor to system noise, and the optimal intensities for the pump and probe were determined. In communication experiments, the T_x antenna was placed at 5 m from the receiver (RFAM) in line of sight with its aperture facing along the z direction. The power consumption during transmission was estimated at 0.45 W, while the corresponding magnetic field measured beside the vapor cell was approximately 4 nT. The measured EVM and SNR were 7% and 30.6 dB, respectively, at 150 sym/s. These findings demonstrate the potential of using multi-resonant antennas and an RFAM for communication over electrically conductive media. Further research may facilitate the development of compact and portable RFAM systems for magnetic-field-based communications in harsh environments.

CONFLICT OF INTEREST STATEMENT

The authors declare that there is no conflicts of interest.

ORCID

Hyun Joon Lee https://orcid.org/0000-0001-8614-7115
Jang-Yeol Kim https://orcid.org/0000-0003-0644-8087
In-Kui Cho https://orcid.org/0000-0002-4270-6824

REFERENCES

1. C. J. Berglund, L. R. Hunter, D. Krause, Jr, E. O. Prigge, M. S. Ronfeldt, and S. K. Lamoreaux, *New limits on local Lorentz invariance from Hg and Cs magnetometers*, Phys. Rev. Lett. **75** (1995), 1879–1882.
2. D. Bear, R. E. Stoner, R. L. Walsworth, V. A. Kostelecký, and C. D. Lane, *Limit on Lorentz and CPT violation of the neutron using a two-species noble-gas maser*, Phys. Rev. Lett. **85** (2000), 5038–5041.
3. M. N. Nabighian, V. J. Grauch, R. O. Hansen, T. R. LaFehr, Y. Li, J. W. Peirce, J. D. Phillips, and M. E. Ruder, *The historical development of the magnetic method in exploration*, Geophysics **70** (2005), 33ND–61ND.
4. V. Mathé, F. Lévêque, P.-E. Mathé, C. Chevallier, and Y. Pons, *Soil anomaly mapping using a cesium magnetometer: limits in the low magnetic amplitude case*, J. Appl. Geophys. **58** (2006), 202–217.
5. S. K. Lee, M. Mößle, W. Myers, N. Kelso, A. H. Trabesinger, A. Pines, and J. Clarke, *SQUID-detected MRI at 132 μT with T_1-weighted contrast established at 10 μT–300 mT*, Magn. Reson. Med. **53** (2005), 9–14.
6. S. Busch, M. Hatridge, M. Mößle, W. Myers, T. Wong, M. Mück, K. Chew, K. Kuchinsky, J. Simko, and J. Clarke, *Measurements of T_1-relaxation in ex vivo prostate tissue at 132 μT*, Magn. Reson. Med. **67** (2012), 1138–1145.
7. H. J. Lee, S. J. Lee, J. H. Shim, H. S. Moon, and K. Kim, *In-situ Overhauser-enhanced nuclear magnetic resonance at less than 1 μT using an atomic magnetometer*, J. Magn. Reson. **300** (2019), 149–152.
8. I. Hilschenz, S. Oh, S. J. Lee, K. K. Yu, S. M. Hwang, K. Kim, and J. H. Shim, *Dynamic nuclear polarisation of liquids at one microtesla using circularly polarised RF with application to millimetre resolution MRI*, J. Magn. Reson. **305** (2019), 138–145.
9. S. J. Lee, K. Jeong, J. H. Shim, H. J. Lee, S. Min, H. Chae, S. K. Namgoong, and K. Kim, *SQUID-based ultralow-field MRI of a hyperpolarized material using signal amplification by reversible exchange*, Sci. Rep. **9** (2019), 12422.
10. I. F. Akyildiz, P. Wang, and Z. Sun, *Realizing underwater communication through magnetic induction*, IEEE Commun. Mag. **53** (2015), 42–48.
11. A. Pal and K. Kant, *NFMI: near field magnetic induction based communication*, Comput. Netw. **181** (2020), 107548.
12. J. Lee, H. J. Lee, J. Y. Kim, and I. K. Cho, *Gaped two-loop antenna-based magnetic transceiver with an empirical model for wireless underground communication*, IEEE Access **9** (2021), 34962–34974.
13. J. Y. Kim, H. J. Lee, J. H. Lee, J. H. Oh, and I. K. Cho, *Experimental assessment of a magnetic induction-based receiver for magnetic communication*, IEEE Access **10** (2022), 110076–110087.
14. J. Y. Kim, I. K. Cho, H. J. Lee, J. Lee, J. I. Moon, S. M. Kim, S. W. Kim, S. Ahn, and K. Kim, *A novel experimental approach to the applicability of high-sensitivity giant magneto-impedance sensors in magnetic field communication*, IEEE Access **8** (2020), 193091–193101.
15. V. Gerginov, F. C. S. da Silva, and D. Howe, *Prospects for magnetic field communications and location using quantum sensors*, Rev. Sci. Instrum. **88** (2017), 125005.
16. S. J. Ingleby, I. C. Chalmers, T. E. Dyer, P. F. Griffin, and E. Riis, Resonant very low- and ultra low frequency digital signal reception using a portable atomic magnetometer, arXiv Preprint, (2020).
17. V. Gerginov, *Field-polarization sensitivity in RF atomic magnetometers*, Phys. Rev. Appl. **11** (2019), 024008.
18. I. Fan, S. Knappe, and V. Gerginov, *Magnetic communication by polarization helicity modulation using atomic magnetometers*, Rev. Sci. Instrum. **93** (2022), 053004.

19. M. Tahir, I. Ali, P. Yan, M. R. Jafri, J. Zexin, and D. Xiaoqiang, *Exploiting W. Ellison model for seawater communication at gigahertz frequencies based on world ocean atlas data*, ETRI J. **42** (2020), 575–584.
20. T. E. Abrudan, O. Kypris, N. Trigoni, and A. Markham, *Impact of rocks and minerals on underground magneto-inductive communication and localization*, IEEE Access **4** (2016), 3999–4010.
21. I. M. Savukov, S. J. Seltzer, and M. V. Romalis, *Detection of NMR signals with a radio-frequency atomic magnetometer*, J. Magn. Reson. **185** (2007), 214–220.
22. D. A. Keder, D. W. Prescott, A. W. Conovaloff, and K. L. Sauer, *An unshielded radio-frequency atomic magnetometer with sub-femtoTesla sensitivity*, AIP Adv. **4** (2014), 127159.
23. I. Savukov, T. Karaulanov, and M. G. Boshier, *Ultra-sensitive high-density Rb-87 radio-frequency magnetometer*, Appl. Phys. Lett. **104** (2014), 023504.
24. C. Deans, L. Marmugi, and F. Renzoni, *Sub-picotesla widely tunable atomic magnetometer operating at room-temperature in unshielded environments*, Rev. Sci. Instrum. **89** (2018), 083111.
25. H. Yao, B. Maddox, and F. Renzoni, *High-sensitivity operation of an unshielded single cell radio-frequency atomic magnetometer*, Opt. Express **30** (2022), 42015–42025.
26. IEEE Standard for Information Technology—telecommunications and information exchange between systems—local and metropolitan area networks—specific requirements—Part 11: Wireless LAN Medium Access Control (MAC) and Physical Layer (PHY) specifications, IEEE Standard 802.11ac, 2013.

AUTHOR BIOGRAPHIES

Hyun Joon Lee received his BS, MS, and PhD degrees from the Department of Physics, Pusan National University, Busan, Republic of Korea, in 2008, 2011, and 2018, respectively. Between 2018 and 2019, he was a postdoctoral associate at the Korea Research Institute of Standards and Science, where he worked on optical magnetometry. Since 2019, he has been with the Electronics and Telecommunications Research Institute, Daejeon, Republic of Korea. His research interests include ultralow-field magnetic resonance and the development of highly sensitive quantum sensors.

Jung Hoon Oh received his BS degree in Electronics from Kyungpook National University, Daegu, Republic of Korea, in 1997 and his MS degree in Electronic Engineering from the Korea Advanced Institute of Science and Technology, Daejeon, Republic of Korea, in 1999. He is currently working at the Electronics and Telecommunications Research Institute in Daejeon, Republic of Korea. His research interests include magnetic field communications in extreme environments and atomic-based electric field measurements.

Jang-Yeol Kim received his BS, MS, and PhD degrees in Information and Communication Engineering from Chungbuk National University, Cheongju, Republic of Korea, in 2010, 2012, and 2017, respectively. Since 2012, he has been working with the Electronics Telecommunications Research Institute, Daejeon, Republic of Korea. His research interests include antenna design, thermal therapy algorithms, microwave sensing, electromagnetic sensors, and magnetic transceiver systems.

In-Kui Cho received his BS and MS degrees from the Department of Electronic Engineering, Kyungpook National University, Daegu, Republic of Korea, in 1997 and 1999, respectively, and his PhD degree in Electrical Engineering from the Korean Advanced Institute of Science and Technology, Daejeon, Republic of Korea, in 2007. Since May 1999, he has been with the Electronics and Telecommunications Research Institute, Daejeon, Republic of Korea, where he has designed and developed an optical backplane, optical chip-to-chip interconnect system, and magnetic-resonance wireless power transfer system. His current research interests include the simulation and development of wireless power transfer components and magnetic field communications through devices such as planar magnetic resonators, magnetic resonators for three-dimensional wireless power transfer and electromagnetic sensors, and magnetic transceiver systems.

How to cite this article: H. J. Lee, J. H. Oh, J.-Y. Kim, and I.-K. Cho, *Performance analysis of atomic magnetometer and bandwidth-extended loop antenna in resonant phase-modulated magnetic field communication system*, ETRI Journal (2023), 1–10, DOI 10.4218/etrij.2023-0156.